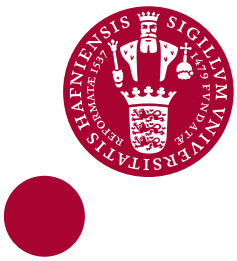

The Radius-Luminosity Relationship for Active Galactic Nuclei

The Effect of Host-Galaxy Starlight on Luminosity Measurements

Bentz, Misty C.; Peterson, Bradley M.; Pogge, Richard W.; Vestergaard, Marianne; Onken, Christopher A.

Published in:
Astrophysical Journal

DOI:
10.1086/503537

Publication date:
2006

The Radius–Luminosity Relationship for Active Galactic Nuclei: The Effect of Host-Galaxy Starlight on Luminosity Measurements

Misty C. Bentz[1], Bradley M. Peterson[1], Richard W. Pogge[1], Marianne Vestergaard[2], and Christopher A. Onken[1,3]

ABSTRACT

We have obtained high resolution images of the central regions of 14 reverberation-mapped active galactic nuclei (AGN) using the *Hubble Space Telescope* Advanced Camera for Surveys High Resolution Camera to account for host-galaxy starlight contamination of measured AGN luminosities. We measure the host-galaxy starlight contribution to the continuum luminosity at 5100 Å through the typical ground-based slit position and geometry used in the reverberation-mapping campaigns. We find that removing the starlight contribution results in a significant correction to the luminosity of each AGN, both for lower luminosity sources, as expected, but also for the higher luminosity sources such as the PG quasars. After accounting for the host galaxy starlight, we revisit the well-known broad-line region radius–luminosity relationship for nearby AGN. We find the power-law slope of the relationship for the Hβ line to be 0.518 ± 0.039, shallower than previously reported and consistent with the slope of 0.5 expected from the naive theoretical assumption that all AGN have, on average, the same ionizing spectrum and the same ionization parameter and gas density in the Hβ line-emitting region.

Subject headings: galaxies: active — galaxies: nuclei — galaxies: photometry — galaxies: Seyfert

[1]Department of Astronomy, The Ohio State University, 140 West 18th Avenue, Columbus, OH 43210; bentz, peterson, pogge@astronomy.ohio-state.edu

[2]Steward Observatory, The University of Arizona, 933 North Cherry Avenue, Tucson, AZ 85721; mvestergaard@as.arizona.edu

[3]Present address: National Research Council Canada, Herzberg Institute of Astrophysics, 5071 West Saanich Road, Victoria, BC V9E 2E7; christopher.onken@nrc-cnrc.gc.ca

1. INTRODUCTION

Over the past 15 years, reverberation-mapping (Blandford & McKee 1982; Peterson 1993) efforts have led to measurements of the size of the broad-line region (BLR), and consequently black hole mass measurements, for 36 Seyfert 1 galaxies and low-luminosity quasars (Peterson et al. 2004, 2005). Early efforts began with individual objects and soon composed a handful of bright, relatively nearby Seyfert galaxies (see Koratkar & Gaskell 1991b and references therein for a summary of early work). Two very important relationships were anticipated and searched for (e.g. Koratkar & Gaskell 1991a): the radius–luminosity (r–L) relationship (the relationship between the BLR size and optical luminosity of the AGN) and the mass–luminosity relationship (the relationship between the mass of the central black hole and the optical luminosity). While the r–L relationship was detectable in Seyfert 1 galaxies alone (Peterson 1993), it was the addition of 17 quasars from the Palomar-Green (PG) sample (Schmidt & Green 1983) that allowed these relationships to be studied in detail, as the larger range of luminosities allowed for the emergence of a statistically significant correlation (Kaspi et al. 2000).

With a calibrated r–L relationship, one can quickly estimate black hole masses for large numbers of AGN with only two spectral measurements: the velocity width of an emission line (usually Hβ) and the continuum luminosity as a proxy for the radius. This method of estimating masses is especially useful for high redshift sources where reverberation-mapping is impractical or impossible (Wandel et al. 1999; Vestergaard 2002, 2004; McLure & Jarvis 2002; Wu et al. 2004; see also Vestergaard & Peterson 2006). Understanding the growth of black holes throughout cosmic history is a key step to understanding the evolution of galaxies and the universe, so correctly calibrating the r–L relationship is crucial. In addition, a correct calibration is necessary for understanding the physics of the central regions of AGN, such as the ionization parameter, the ionizing spectral energy distribution (SED), the gas density, and the column density. These parameters are inferred from the form of the r–L relationship, and our understanding of them relies heavily on the accuracy with which the r–L relationship is known.

Recently, Peterson et al. (2004) compiled and consistently reanalyzed all available reverberation-mapping data for 35 AGN to improve their black hole mass measurements. Subsequently, the r–L relationship was reexamined by Kaspi et al. (2005). Assuming a power-law relationship $R_{BLR} \propto L^{\alpha}$, they find a best-fit value of $\alpha = 0.665 \pm 0.069$ using the optical continuum and broad Hβ line. However, some of the nearby AGN have host galaxy starlight luminosities that are comparable to the luminosities of their central sources. With the relatively large apertures used during the AGN monitoring campaigns (typically on the order of $5\farcs0 \times 7\farcs5$), the host-galaxy starlight contribution is substantial. Ignoring the

starlight contribution to the optical luminosity will overestimate the optical luminosity of the source and artificially steepen the slope of the r–L relationship, as the starlight fraction is relatively more important in the lower luminosity objects.

Previous attempts to quantify the host-galaxy starlight contribution to the optical flux at 5100 Å were carried out using ground-based telescopes with $1-2''$ seeing (Alloin et al. 1995; Stirpe et al. 1994; Peterson et al. 1995; Romanishin et al. 1995). However, the relatively low resolution available from the ground of even the most nearby sources, coupled with seeing effects on the order of $1''$, make it almost impossible to disentangle the nucleus and the bulge of the galaxy. In this paper, we use high resolution *Hubble Space Telescope* (HST) images to measure the contribution from starlight to previous luminosity measurements of 14 reverberation-mapped AGN and we present a revised r–L relationship in which these effects are taken into account.

2. OBSERVATIONS AND DATA REDUCTION

Between 2003 August 22 and 2004 May 28, we observed 14 Seyfert 1 galaxies with the *HST* Advanced Camera for Surveys (ACS) in Snapshot mode. The targets and details of the observations are listed in Table 1. Each object was imaged with the High Resolution Camera (HRC) through the F550M filter ($\lambda_c = 5580$ Å and $\Delta\lambda = 547$ Å), thereby probing the continuum while avoiding strong emission lines. The observations consisted of three exposures for each object with exposure times of 120 s, 300 s, and 600 s. This method of graduating the exposure times was employed to avoid saturation of the nucleus but still obtain a reasonable signal-to-noise ratio (S/N) for the wings of the point-spread function (PSF) and the host galaxy. Each individual exposure was split into two equal sub-exposures to facilitate the rejection of cosmic rays (see e.g. Carollo et al. 1997; Ho & Peng 2001 for discussions of the challenges involved in obtaining accurate optical photometric data of faint nuclei in bright nearby galaxies).

The nuclei of most of the 600 s exposures were saturated, and the nuclei of the 300 s observations of NGC 3783 and PG 0844+349 were also saturated. Only 3C 390.3, Fairall 9, Mrk 110, Mrk 590, and NGC 5548 were unsaturated in all three graduated exposures.

The data quality frames provided by the *HST* pipeline were consulted to identify the individual saturated pixels associated with the nucleus in each exposure frame. These saturated pixels were clipped from the image and replaced by the same pixels from a non-saturated exposure after scaling them by the relative exposure times. The three frames for each object were then summed to give one frame with an effective exposure time of 1020 s for each of

the 14 objects.

Cosmic rays were identified in the summed images with the Laplacian cosmic ray identification package L.A.Cosmic (van Dokkum 2001). Pixels in the PSF area of each image that were identified by L.A.Cosmic were excluded from the list of affected pixels prior to cleaning with XVista.[1] Each remaining affected pixel was replaced with the median value for the eight pixels immediately surrounding it.

Finally, the summed, cleaned images were corrected for the distortions of the ACS camera with the PyRAF routine *pydrizzle* in the STSDAS[2] package for IRAF[3].

The final images for four representative galaxies — 3C 120, 3C 390.3, NGC 3227, and NGC 5548 — are shown in Figure 1, overlaid with the apertures that were used in their ground-based monitoring campaigns.

3. GALAXY DECOMPOSITION

Each object was fit with typical spiral galaxy parameters in order to determine and accurately subtract the contribution from the central point source. The galaxies were modeled using the two-dimensional image decomposition program Galfit (Peng et al. 2002), which fits analytic functions for the bulge and disk, plus an additional point source for the nucleus, convolved with a user-supplied model PSF. The simulated PSF was created using the TinyTim package (Krist 1993), which models the optics of *HST* plus the specifics of the camera and filter system.

Several initial attempts to fit the galaxies led to the following relatively robust models for the individual components of each galaxy: bulges were fit with a de Vaucouleurs (1948) $R^{1/4}$ profile, disks were fit with an exponential model, and the central PSF was created using TinyTim as discussed above. Each parameter governing the models was allowed to vary from the initial conditions except the boxy/disky parameter, which sometimes led to instabilities in the fits and was therefore held fixed at zero for each of the fits. Figure 2 shows the galaxy

[1]XVISTA was originally developed as Lick Observatory Vista and is now maintained in the public domain by former Lick graduate students as a service to the community. It is currently maintained by Jon Holtzman at New Mexico State University, and is available at http://ganymede.nmsu.edu/holtz/xvista.

[2]STSDAS and PyRAF are products of the Space Telescope Science Institute, which is operated by AURA for NASA.

[3]IRAF is distributed by the National Optical Astronomical Observatory, which is operated by the Association of Universities for Research in Astronomy, Inc., under cooperative agreement with the NSF.

fits and residuals for the four representative objects — 3C 120, 3C 390.3, NGC 3227, and NGC 5548 — spanning the range of fit quality encountered for the various angular sizes of objects in our sample.

Once the fits were relatively stable from perturbations on the initial conditions, the best-fit central PSFs were subtracted from the images, resulting in a nucleus-free image of each of the 14 objects, which are shown in Figure 3. Below, we describe the detailed results of the fits to individual galaxies.

3C 120. A central PSF, a deVaucouleurs profile, and an exponential disk were fitted to 3C 120, resulting in a rather clean subtraction. A tidal tail west of the nucleus and trailing to the north remains in the residuals (see Figure 2).

3C 390.3. We fit 3C 390.3 with a central PSF, a deVaucouleurs profile, and an exponential disk. The residuals are the cleanest for any of the 14 objects in this particular sample and reveal no evidence for any underlying structure (see Figure 2).

Fairall 9. A central PSF, a deVaucouleurs profile, and an exponential disk was fit to Fairall 9. A strong bar oriented in the east–west direction is clearly evident in the fit residuals for Fairall 9.

Markarian 110. The fit for Markarian 110 included only a central PSF and a deVaucouleurs profile, as the disk surface brightness was evidently too low to be detected in these observations. The apparent double nucleus, the result of a foreground star superimposed on the galaxy to the northeast of the central source (Hutchings & Craven 1988), is clearly resolved in the images, and the residuals are very clean with no evidence for any additional underlying structure.

Markarian 279. We fit Markarian 279 with a central PSF, a deVaucouleurs profile, and an exponential disk. Faint spiral arms are visible in the fit residuals.

Markarian 590. Only a central PSF and a deVaucouleurs profile were fit to Markarian 590. There appears to be a rather bright bar in the center of the galaxy on a scale of approximately 3–4″ and the spiral arms appear to penetrate all the way to the very nucleus of the galaxy, although whether the inner spiral arms are connected to the outer spiral arms is unclear.

Markarian 817. We fit Markarian 817 with a central PSF, a deVaucouleurs profile, and an exponential disk. The residuals clearly show the central bar and two tightly wound spiral arms.

NGC 3227. The fit for NGC 3227 was one of the most marginal fits we encountered. It included a central PSF, a deVaucouleurs profile, and an exponential disk. The large amounts of dust in the center of the galaxy make for an interesting residual image (see Figure 2).

NGC 3783. A central PSF, a deVaucouleurs profile, and an exponential disk were fit to NGC 3783. There appears to be faint evidence for a bar at a position angle (PA) of roughly 160°.

NGC 4051. We fit NGC 4051 with a central PSF, a deVaucouleurs profile, and an exponential disk. The residuals show a bright circumnuclear ring as well as areas of dust absorption.

NGC 4151. The fit for NGC 4151 included a central PSF, a deVaucouleurs profile, and an exponential disk. The residuals show a fairly messy central region with dust absorption and areas of excess luminosity.

NGC 5548. A central PSF, a deVaucouleurs profile, and an exponential disk were fit to NGC 5548. The spiral arms are clearly visible in the residuals, as well as various knots of star formation in the arms (see Figure 2).

PG 0844+349. We fit PG 0844+349 with a central PSF, a deVaucouleurs profile, and an exponential disk. The residuals are very clean and show no evidence for underlying structure.

PG 2130+099. Only a central PSF and a deVaucouleurs profile were necessary to fit PG 2130+099. The residuals are fairly clean but hint at a tidal tail trailing towards the west.

4. FLUX MEASUREMENTS

The nucleus-free image of each galaxy was overlaid with the typical aperture used in its ground-based monitoring program at the typical orientation and centered on the position of the AGN (see Table 2). The counts within the aperture were summed and converted to f_λ flux density units (erg s^{-1} cm^{-2} Å^{-1}) using the *HST* keyword PHOTFLAM and the effective exposure time for each object.

Color corrections between the flux observed through the *HST* F550M filter and rest-frame 5100 Å were calculated using a model bulge spectrum (Kinney et al. 1996) plus a powerlaw component of the form $f_\nu \propto \nu^{-0.5}$ for the AGN component. The relative amounts of emission from each of the two components were set by the measured fractions of bulge and AGN emission in each combined *HST* image. All of the color corrections were close to one. Following Kaspi et al. (2005), we corrected for galactic absorption using the Schlegel et al. (1998) $E(B-V)$ values listed in the NASA/IPAC Extragalactic Database (NED) and the extinction curve of Cardelli et al. (1989), adjusted to $A_V/E(B-V) = 3.1$. Table 3 lists the color correction for each galaxy as the ratio of the flux at restframe 5100 Å to the average flux through the *HST* F550M filter, as well as the final host-galaxy flux measurement at 5100 Å for each galaxy through the monitoring aperture listed in Table 2.

It is interesting to note that these galaxy flux measurements are not in good agreement with previous measurements made from the ground in a similar fashion (see Table 3). Our own ground-based tests with the 1.3-m McGraw-Hill Telescope at MDM Observatory revealed that the typical resolution achieved from the ground coupled with the 1-2 ″ seeing typical of ground-based projects resulted in the PSF of the central source and the bulge smearing together in an indistinguishable fashion. Our attempts to fit the galaxy with ground-based images were more dependent on the initial parameters supplied to Galfit than on any information in the images themselves. Therefore, we strongly recommend that future projects rely only on high spatial resolution images such as those acquired with space-based or diffraction-limited telescopes.

5. THE RADIUS-LUMINOSITY RELATIONSHIP

We have calculated several types of fits to the r–L relationship for the 35 reverberation-mapped AGN after correcting the above 14 for starlight from the host galaxy. These calculations will be refined in the future as we correct additional reverberation-mapped AGN for host-galaxy starlight contributions. Following Kaspi et al. (2005), the r–L fits have been calculated for the Hβ line only as well as for the Balmer-line average. Within these divisions,

we have also made the distinction of treating each separate measurement of an object individually, as well as taking the mean of multiple measurements weighted by the average of the positive and negative errors. We tested the differences between weighting measurements by the average of their errors, by taking only the positive errors, and by taking the errors toward the fit in the manner of Kaspi et al. (2005). We find the differences in these weighting methods to be at the 2% level, and therefore negligible.

For those fits that used only the Hβ BLR radius, three objects (PG 0844+349, PG 1211+143, and NGC 4593) were determined by Peterson et al. (2004) to have unreliable Hβ time delays and these objects are therefore excluded from any fits to the Hβ r–L relationship. Other fits excluded NGC 3516, IC 4329A, and NGC 7469 because they have a significant, but unquantified, host-galaxy starlight contribution that we are unable to correct for at this time.[4] For some fits, we also excluded NGC 3227 and NGC 4051, as they are well known to have significant nuclear structure and reddening, as well as PG 2130+099, which is a clear outlier and for which we now believe the radius measurement is probably erroneous (this will be discussed elsewhere in more detail).

We have used three different methods to calculate the relationship between the size of the BLR and the optical luminosity:

1. FITEXY (Press et al. 1992), which estimates the parameters of a straight-line fit through the data including errors in both coordinates. FITEXY numerically solves for the minimum orthogonal χ^2 using an interative root-finding algorithm. We include intrinsic scatter similar to Kaspi et al. (2005). Namely, the fractional scatter listed in Table 5 is the fraction of the measurement value of r (not the error value) that is added in quadrature to the error value so as to obtain a reduced χ^2 of 1.0.

2. BCES (Akritas & Bershady 1996), which attempts to account for the effects of errors on both coordinates in the fit using bivariate correlated errors, including a component of intrinsic scatter. We adopt the bootstrap of the bisector value following Kaspi et al. (2005).

3. GaussFit (McArthur et al. 1994), which implements generalized least-squares using robust Householder Orthogonal Transformations (Jefferys 1980, 1981) to solve the non-linear equations of condition for the problem of errors in both coordinates.

[4]We have an approved *HST* Cycle 14 program to quantify the starlight contribution from these objects in the same manner as the objects examined in this work.

Table 4 lists the previous luminosity measurement (Kaspi et al. 2005), the luminosity after correction for host-galaxy starlight, and the Hβ time lag data (Peterson et al. 2004) for each of the 14 reverberation-mapped AGN in this study. For the remaining 21 reverberation-mapped AGN that were not corrected in this work, their Hβ time lags can be found in Table 6 of Peterson et al. (2004) and their luminosities and Balmer-line averaged time lags are available in Table 1 of Kaspi et al. (2005).

Table 5 lists the various fits to the r–L relationship for each of the fitting methods discussed above. The fit parameters listed in Table 5 are appropriate for fits to the function:

$$\log\left(R_{\rm BLR}\right) = K + \alpha \log\left(\lambda L_{\lambda}\left(5100\text{Å}\right)\right) \tag{1}$$

where α is the slope of the power-law relationship between $R_{\rm BLR}$ and $L\left(5100\,\text{Å}\right)$ and K is the scaling factor.

It is easily observed that the calculated slope of the r–L relationship in Table 5 does not depend sensitively on the fitting method employed or the inclusion or exclusion of certain suspect data points. For the remainder of this paper we will adopt the best-fit parameters calculated using GaussFit, shown in bold face in Table 5 and plotted in Figure 4 against the best fit determined by Kaspi et al. (2005). The generalized least-squares method of Jefferys (1980, 1981) implemented by GaussFit has the virtue of directly addressing the explicit non-linearity of the problem of fitting lines through data with errors in both variables, whereas BCES and FITEXY use iterative linear approximations to estimate the best-fit parameters. We used these latter two methods only because they were employed by Kaspi et al. (2005), and this allows us to make a more direct comparison with their results.

6. DISCUSSION

The first models of the BLRs of AGN were modified from planetary nebulae models, as the emitting gas in the first studied AGN looked somewhat similar to the clouds or filaments of nebulae (Greenstein & Schmidt 1964). This typical BLR model of optically thick, line-emitting gas did not change significantly for several years (see the review by Davidson & Netzer 1979). Eventually, various other models of the BLR were added. They included cool clouds embedded in hot gas (Krolik et al. 1981), bloated stars (Scoville & Norman 1988; Kazanas 1989; Alexander & Netzer 1994), magnetically-driven disk winds (Emmering et al. 1992), and the combination of disk and disk wind components (Murray et al. 1995).

Photoionization equilibrium codes have often been employed to study the basic charac-

teristics of the BLR as observed through the AGN spectra (early versions: Davidson 1977; Davidson & Netzer 1979; Kwan & Krolik 1981; later versions: Rees et al. 1989; Goad et al. 1993; Kaspi & Netzer 1999; Baldwin et al. 1995; Korista & Goad 2000). Typically, the line-emitting gas clouds are parameterized by elemental abundance, the shape of the ionizing continuum, and an ionization parameter

$$U = \frac{Q(H)}{4\pi r^2 c n_e} \ , \tag{2}$$

where

$$Q(H) = \int_{\nu_1}^{\infty} \frac{L_\nu}{h\nu}\, d\nu \tag{3}$$

is the number of photons with energies in excess of $h\nu_1 = 13.6$ eV (the energy required to ionize hydrogen) emitted each second by the central source.

To the lowest order, all AGN spectra are remarkably similar.[5] Therefore, one can assume that the ionization parameters and particle densities are about the same for all AGN. Rearranging the definition of the ionization parameter U, we find:

$$r = \left(\frac{Q(H)}{4\pi c n_e U}\right)^{1/2} \propto Q(H)^{1/2}. \tag{4}$$

If we further assume that the shape of the ionizing continuum is not a function of luminosity, then $L \propto Q(H)$ so that

$$r \propto L^{1/2} \tag{5}$$

and therefore we can expect the slope of the r–L relationship to be $\alpha \approx 0.5$.

Accounting for host-galaxy starlight emission in the 14 objects with high resolution *HST* imaging, we find a significant deviation from the r–L fit parameters published by Kaspi et al. (2005). Figure 4 shows both the previous r–L fit found by Kaspi et al. (2005) as well as the

[5]For a visual representation of this remarkable fact, see the luminosity-binned composite spectra from the Sloan Digital Sky Survey presented by vanden Berk et al. (2004). The largest differences between the composites are due to the "Baldwin Effect" — the C IV λ1549 emission line decreases in equivalent width as the continuum luminosity increases (Baldwin 1977).

new fit that we present here. Comparing the Hβ r–L fit, where multiple measurements are averaged together, Kaspi et al. (2005) quote a power-law slope of $\alpha = 0.665 \pm 0.069$, while we find a power-law slope of $\alpha = 0.518 \pm 0.039$ when excluding any sources with significant but unquantified host galaxy emission or strong reddening. Our value of the slope is in good agreement with the expectation of $\alpha = 0.5$, based on the naive assumptions that the ionization parameters, gas densities, and ionizing SEDs of all AGNs are the same.

7. CONCLUSIONS

We have measured the host-galaxy starlight component to previous luminosity measurements of 14 reverberation-mapped AGN through their original monitoring apertures. Removing the starlight component from the luminosity measurements, we recalculate the r–L relationship for nearby AGN. Regardless of the detailed selection of the sample or the regression method used to determine the fit, we find a slope of $\alpha \approx 0.50$ for Hβ and $\alpha \approx 0.51$ for the mean of the Balmer lines, both consistent with the naive photoionization expectation of $\alpha = 0.5$ if all AGN have the same ionization parameter, gas density, and ionizing SED.

Additional high-resolution optical imaging by *HST* is necessary to constrain the amount of host-galaxy starlight contribution to the remaining population of reverberation-mapped AGN, and we are therefore continuing this investigation.

Better constraints on the Hβ BLR radius are also necessary for many of these objects and additional reverberation experiments are being undertaken.

In order to constrain the true nature of the relationship between the BLR radius and luminosity of the bright AGN in the local universe, each of the objects contributing to the fit of this relationship must be studied and understood in as much detail as possible. A thorough understanding of the local form of this relationship, especially its biases or weaknesses, is crucial if we are to apply it in the hopes of understanding the growth and evolution of AGN and galaxies from the early universe to the present day.

We would like to thank an anonymous referee for comments that improved the presentation of this paper. This work is based on observations with the NASA/ESA *Hubble Space Telescope*. We are grateful for support of this work through grant *HST* GO-9851 from the Space Telescope Science Institute, which is operated by the Association of Universities for Research in Astronomy, Inc., under NASA contract NAS5-26555, and by the NSF through grant AST-0205964 to The Ohio State University. M.B. is supported by a Graduate Fellowship from the National Science Foundation. M.V. acknowledges financial support from

NSF grant AST-0307384 to the University of Arizona. This research has made use of the NASA/IPAC Extragalactic Database (NED) which is operated by the Jet Propulsion Laboratory, California Institute of Technology, under contract with the National Aeronautics and Space Administration and the SIMBAD database, operated at CDS, Strasbourg, France.

REFERENCES

Akritas, M. G., & Bershady, M. A. 1996, ApJ, 470, 706

Alexander, T., & Netzer, H. 1994, MNRAS, 270, 781

Alloin, D., et al. 1995, A&A, 293, 293

Baldwin, J., Ferland, G., Korista, K., & Verner, D. 1995, ApJ, 455, L119

Baldwin, J. A. 1977, ApJ, 214, 679

Blandford, R. D., & McKee, C. F. 1982, ApJ, 255, 419

Cardelli, J. A., Clayton, G. C., & Mathis, J. S. 1989, ApJ, 345, 245

Carollo, C. M., Stiavelli, M., de Zeeuw, P. T., & Mack, J. 1997, AJ, 114, 2366

Davidson, K. 1977, ApJ, 218, 20

Davidson, K., & Netzer, H. 1979, Reviews of Modern Physics, 51, 715

de Vaucouleurs, G. 1948, Annales d'Astrophysique, 11, 247

Dietrich, M., et al. 1998, ApJS, 115, 185

Emmering, R. T., Blandford, R. D., & Shlosman, I. 1992, ApJ, 385, 460

Goad, M. R., O'Brien, P. T., & Gondhalekar, P. M. 1993, MNRAS, 263, 149

Greenstein, J. L., & Schmidt, M. 1964, ApJ, 140, 1

Ho, L. C., & Peng, C. Y. 2001, ApJ, 555, 650

Hutchings, J. B., & Craven, S. E. 1988, AJ, 95, 677

Jefferys, W. H. 1980, AJ, 85, 177

Jefferys, W. H. 1981, AJ, 86, 149

Kaspi, S., Maoz, D., Netzer, H., Peterson, B. M., Vestergaard, M., & Jannuzi, B. T. 2005, ApJ, 629, 61

Kaspi, S., & Netzer, H. 1999, ApJ, 524, 71

Kaspi, S., Smith, P. S., Netzer, H., Maoz, D., Jannuzi, B. T., & Giveon, U. 2000, ApJ, 533, 631

Kaspi, S., et al. 1996, ApJ, 470, 336

Kazanas, D. 1989, ApJ, 347, 74

Kinney, A. L., Calzetti, D., Bohlin, R. C., McQuade, K., Storchi-Bergmann, T., & Schmitt, H. R. 1996, ApJ, 467, 38

Koratkar, A. P., & Gaskell, C. M. 1991a, ApJ, 370, L61

—. 1991b, ApJS, 75, 719

Korista, K. T., & Goad, M. R. 2000, ApJ, 536, 284

Krist, J. 1993, in ASP Conf. Ser. 52: Astronomical Data Analysis Software and Systems II, 536

Krolik, J. H., McKee, C. F., & Tarter, C. B. 1981, ApJ, 249, 422

Kwan, J., & Krolik, J. H. 1981, ApJ, 250, 478

Maoz, D., Netzer, H., Leibowitz, E., Brosch, N., Laor, A., Mendelson, H., Beck, S., Almoznino, E., & Mazeh, T. 1990, ApJ, 351, 75

Maoz, D., Netzer, H., Mazeh, T., Beck, S., Almoznino, E., Leibowitz, E., Brosch, N., Mendelson, H., & Laor, A. 1991, ApJ, 367, 493

McArthur, B., Jefferys, W., & McCartney, J. 1994, Bulletin of the American Astronomical Society, 26, 900

McLure, R. J., & Jarvis, M. J. 2002, MNRAS, 337, 109

Murray, N., Chiang, J., Grossman, S. A., & Voit, G. M. 1995, ApJ, 451, 498

Netzer, H., Maoz, D., Laor, A., Mendelson, H., Brosch, N., Leibowitz, E., Almoznino, E., Beck, S., & Mazeh, T. 1990, ApJ, 353, 108

Onken, C. A., & Peterson, B. M. 2002, ApJ, 572, 746

Onken, C. A., Peterson, B. M., Dietrich, M., Robinson, A., & Salamanca, I. M. 2003, ApJ, 585, 121

Peng, C. Y., Ho, L. C., Impey, C. D., & Rix, H. 2002, AJ, 124, 266

Peterson, B. M. 1993, PASP, 105, 247

Peterson, B. M., Pogge, R. W., Wanders, I., Smith, S. M., & Romanishin, W. 1995, PASP, 107, 579

Peterson, B. M., Wanders, I., Bertram, R., Hunley, J. F., Pogge, R. W., & Wagner, R. M. 1998, ApJ, 501, 82

Peterson, B. M., et al. 2000, ApJ, 542, 161

—. 2002, ApJ, 581, 197

—. 2004, ApJ, 613, 682

—. 2005, ApJ, 632, 799 Erratum in press (astro-ph/0506665)

Press, W. H., Teukolsky, S. A., Vetterling, W. T., & Flannery, B. P. 1992, Numerical recipes in FORTRAN. The art of scientific computing (Cambridge: University Press, 2nd ed.), 660

Rees, M. J., Netzer, H., & Ferland, G. J. 1989, ApJ, 347, 640

Romanishin, W., et al. 1995, ApJ, 455, 516

Salamanca, I., et al. 1994, A&A, 282, 742

Santos-Lleó, M., et al. 1997, ApJS, 112, 271

—. 2001, A&A, 369, 57

Schlegel, D. J., Finkbeiner, D. P., & Davis, M. 1998, ApJ, 500, 525

Schmidt, M., & Green, R. F. 1983, ApJ, 269, 352

Scoville, N., & Norman, C. 1988, ApJ, 332, 163

Stirpe, G. M., et al. 1994, ApJ, 425, 609

van Dokkum, P. G. 2001, PASP, 113, 1420

vanden Berk, D., Yip, C., Connolly, A., Jester, S., & Stoughton, C. 2004, in ASP Conf. Ser. 311: AGN Physics with the Sloan Digital Sky Survey, 21–24

Vestergaard, M. 2002, ApJ, 571, 733

—. 2004, ApJ, 601, 676

Vestergaard, M., & Peterson, B. M. 2006, ApJ, in press (astro-ph/0601303)

Wandel, A., Peterson, B. M., & Malkan, M. A. 1999, ApJ, 526, 579

Winge, C., Peterson, B. M., Horne, K., Pogge, R. W., Pastoriza, M. G., & Storchi-Bergmann, T. 1995, ApJ, 445, 680

Wu, X.-B., Wang, R., Kong, M. Z., Liu, F. K., & Han, J. L. 2004, A&A, 424, 793

Table 1. Observation Log

Objects	References[a]	z	D_L (Mpc)	Date Observed (yyyy–mm–dd)	Beginning UTC (hh:mm:ss)	Datasets (J8SC)
Fairall 9	1	0.04702	209	2003-08-22	00:44:00	04011,04021,04031
Mrk 590	2	0.02639	115	2003-12-18	02:27:00	05011,05021,05031
3C 120	2	0.03301	145	2003-12-05	05:48:00	06011,06021,06031
PG 0844+349	3	0.06400	287	2004-05-10	20:11:00	10011,10021,10031
Mrk 110	2	0.03529	155	2004-05-28	17:34:00	11011,11021,11031
NGC 3227	4,5,6	0.00386	17	2004-03-20	04:28:00	13011,13021,13031
NGC 3783	7,8	0.00973	42	2003-11-15	00:11:00	15011,15021,15031
NGC 4051	9	0.00234	10	2004-02-16	01:49:00	16011,16021,16031
NGC 4151	10,11	0.00332	14	2004-03-28	14:25:00	17011,17021,17031
Mrk 279	12,13	0.03045	133	2003-12-07	03:54:00	24011,24021,24031
NGC 5548	14,15	0.01718	75	2004-04-07	01:53:00	27011,27021,27031
Mrk 817	2	0.03146	138	2003-12-08	18:08:00	29011,29021,29031
3C 390.3	16	0.05610	251	2004-03-31	06:56:00	34011,34021,34031
PG 2130+099	3	0.06298	283	2003-10-21	06:47:00	36011,36021,36031

[a]References refer to reverberation-mapping campaigns in optical wavelengths.

References. — 1. Santos-Lleó et al. (1997), 2. Peterson et al. (1998), 3. Kaspi et al. (2000), 4. Salamanca et al. (1994), 5. Onken et al. (2003), 6. Winge et al. (1995), 7. Stirpe et al. (1994), 8. Onken & Peterson (2002), 9. Peterson et al. (2000), 10. Kaspi et al. (1996), 11. Maoz et al. (1991), 12. Santos-Lleó et al. (2001), 13. Maoz et al. (1990), 14. Peterson et al. (2002) and references therein, 15. Netzer et al. (1990), 16. Dietrich et al. (1998),

Table 2. Ground-Based Monitoring Aperture Sizes and Orientations

Object	PA (°)	Aperture (″)	References
Fairall 9	0	4×9	1
Mrk 590	90	5×7.6	2
3C 120	90	5×7.6	2
PG 0844+349	36.8	10×13	3
Mrk 110	90	5×7.6	2
NGC 3227	25	1.5×4	4
NGC 3783	0	5×10	5
NGC 4051	90	5×7.5	6
NGC 4151	156.3	10×13	7
Mrk 279	90	5×7.5	8
NGC 5548	90	5×7.5	9
Mrk 817	90	5×7.6	2
3C 390.3	90	5×7.5	10
PG 2130+099	68.2	10×13	3

References. — 1. Santos-Lleó et al. (1997), 2. Peterson et al. (1998), 3. Kaspi et al. (2000), 4. Salamanca et al. (1994), 5. Stirpe et al. (1994), 6. Peterson et al. (2000), 7. Kaspi et al. (1996), 8. Santos-Lleó et al. (2001), 9. Peterson et al. (2002) and references therein, 10. Dietrich et al. (1998).

Table 3. Galaxy Flux

Object	Color Term $f_{5100\mathring{A}}/f_{F550M}$	$f_{gal}(5100\text{Å})$ [a] (10^{-15} erg s^{-1} cm^{-2} Å^{-1})	$f_{GB}(5100\text{Å})$ [b] (10^{-15} erg s^{-1} cm^{-2} Å^{-1})	References
Fairall 9	1.002	$4.32^{+0.73}_{-0.87}$		
Mrk 590	0.953	$4.83^{+0.81}_{-0.98}$		
3C 120	1.046	$1.82^{+0.31}_{-0.37}$		
PG 0844+349	1.018	$2.66^{+0.45}_{-0.54}$		
Mrk 110	1.076	$1.11^{+0.19}_{-0.23}$		
NGC 3227	1.009	$5.96^{+1.00}_{-1.21}$		
NGC 3783	1.027	$7.60^{+1.28}_{-1.54}$	10.99	1,2
NGC 4051	0.987	$10.43^{+1.75}_{-2.11}$		
NGC 4151	0.960	$29.77^{+5.01}_{-6.02}$	14.0	3
Mrk 279	1.031	$3.68^{+0.62}_{-0.75}$		
NGC 5548	0.965	$4.47^{+0.75}_{-0.90}$	3.4	3,4
Mrk 817	1.030	$2.48^{+0.42}_{-0.50}$		
3C 390.3	1.018	$1.19^{+0.20}_{-0.24}$		
PG 2130+099	1.021	$1.91^{+0.32}_{-0.39}$		

[a]Galaxy fluxes through the apertures described in Table 2 after subtraction of the central sources and color corrections from the *HST* F550M filter to 5100 Å. Fluxes are not corrected for galactic extinction.

[b]Galaxy fluxes in the literature determined from ground-based images.

References. — 1. Alloin et al. (1995), 2. Stirpe et al. (1994), 3. Peterson et al. (1995), 4. Romanishin et al. (1995).

Table 4. Optical Luminosities and Hβ BLR Radii

Object	Previous $\lambda L_\lambda(5100\,\text{Å})$[a] ($10^{44}$ erg s^{-1})	Corrected $\lambda L_\lambda(5100\,\text{Å})$[b] ($10^{44}$ erg s^{-1})	R_{BLR}[c] (lt days)
Fairall 9	1.79 ± 0.20	0.49 ± 0.25	$17.4^{+3.2}_{-4.3}$
Mrk 590	0.736 ± 0.058	0.288 ± 0.066	$20.7^{+3.5}_{-2.7}$
	0.497 ± 0.053	0.0468 ± 0.0978	$14.0^{+8.5}_{-8.8}$
	0.594 ± 0.042	0.145 ± 0.050	$29.2^{+4.9}_{-5.0}$
	0.786 ± 0.122	0.339 ± 0.151	$28.8^{+3.6}_{-4.2}$
3C 120	1.39 ± 0.25	0.851 ± 0.324	$38.1^{+21.3}_{-15.3}$
PG 0844+349	2.21 ± 0.23	0.631 ± 0.281	$3.0^{+12.4}_{-10.0}$ [d]
Mrk 110	0.547 ± 0.057	0.372 ± 0.065	$24.3^{+5.5}_{-8.3}$
	0.628 ± 0.080	0.454 ± 0.086	$20.4^{+10.5}_{-6.3}$
	0.42 ± 0.14	0.246 ± 0.182	$33.3^{+14.9}_{-10.0}$
NGC 3227	0.0256 ± 0.0044	0.0151 ± 0.0053	$8.2^{+5.1}_{-8.4}$
NGC 3783	0.178 ± 0.015	0.0603 ± 0.0174	$10.2^{+3.3}_{-2.3}$
NGC 4051	0.0086 ± 0.0006	0.00191 ± 0.00067	$5.8^{+2.6}_{-1.8}$
NGC 4151	0.1110 ± 0.0064	0.0708 ± 0.0068	$3.1^{+1.3}_{-1.3}$
Mrk 279	0.810 ± 0.082	0.383 ± 0.088	$16.7^{+3.9}_{-3.9}$
NGC 5548	0.362 ± 0.046	0.200 ± 0.052	$19.7^{+1.5}_{-1.5}$
	0.260 ± 0.037	0.102 ± 0.046	$18.6^{+2.1}_{-2.3}$
	0.343 ± 0.034	0.182 ± 0.037	$15.9^{+2.9}_{-2.5}$
	0.246 ± 0.043	0.0832 ± 0.0549	$11.0^{+1.9}_{-2.0}$
	0.331 ± 0.032	0.170 ± 0.034	$13.0^{+1.6}_{-1.4}$
	0.356 ± 0.040	0.195 ± 0.045	$13.4^{+3.8}_{-4.3}$
	0.442 ± 0.037	0.282 ± 0.042	$21.7^{+2.6}_{-2.6}$
	0.386 ± 0.060	0.2224 ± 0.071	$16.4^{+1.2}_{-1.1}$
	0.297 ± 0.033	0.135 ± 0.039	$17.5^{+2.0}_{-1.6}$
	0.492 ± 0.053	0.331 ± 0.058	$26.5^{+4.3}_{-2.2}$
	0.432 ± 0.066	0.269 ± 0.078	$24.8^{+3.2}_{-3.0}$
	0.255 ± 0.044	0.0912 ± 0.0567	$6.5^{+5.7}_{-3.7}$
	0.257 ± 0.032	0.0933 ± 0.0385	$14.3^{+5.9}_{-7.3}$
Mrk 817	0.75 ± 0.10	0.448 ± 0.114	$19.0^{+3.9}_{-3.7}$
	0.61 ± 0.06	0.308 ± 0.062	$15.3^{+3.7}_{-3.5}$

Table 4—Continued

Object	Previous $\lambda L_\lambda(5100\,\text{Å})$[a] ($10^{44}$ erg s^{-1})	Corrected $\lambda L_\lambda(5100\,\text{Å})$[b] ($10^{44}$ erg s^{-1})	R_{BLR}[c] (lt days)
	0.612 ± 0.033	0.310 ± 0.038	$33.6^{+6.5}_{-7.6}$
3C 390.3	0.87 ± 0.14	0.275 ± 0.192	$23.6^{+6.2}_{-6.7}$
PG 2130+099	2.85 ± 0.26	2.24 ± 0.27	$158.1^{+29.8}_{-18.7}$

[a]Continuum luminosity measurements are taken from Table 1 of Kaspi et al. (2005).

[b]Galaxy contributions have been subtracted from corrected luminosities, and Galactic extinction corrections have been applied as described in the text.

[c]BLR radii measurements are calculated using only the Hβ line in the rest frame of the AGN and are taken from Table 6 of Peterson et al. (2004).

[d]This measurement was deemed unreliable by Peterson et al. (2004).

Table 5. BLR r–L Fits

Note	N[a]	FITEXY K	FITEXY α	FITEXY Scatter[b]	BCES K	BCES α	GaussFit K	GaussFit α
				Hβ time lag only				
A	55	-19.9 ± 2.3	0.486 ± 0.052	45	-22.5 ± 2.6	0.546 ± 0.059	-20.3 ± 1.8	0.496 ± 0.041
	32	-22.8 ± 3.2	0.551 ± 0.072	54	-23.7 ± 3.7	0.573 ± 0.082	-21.1 ± 2.4	0.514 ± 0.055
B	52	-19.4 ± 1.6	0.476 ± 0.037	31	-20.0 ± 1.9	0.491 ± 0.044	-19.5 ± 1.4	0.480 ± 0.032
	29	-20.4 ± 2.2	0.499 ± 0.051	38	-20.1 ± 2.6	0.493 ± 0.059	-19.6 ± 1.8	0.482 ± 0.041
C	49	-19.9 ± 1.5	0.487 ± 0.035	26	-21.3 ± 1.5	0.520 ± 0.034	-20.3 ± 1.4	0.496 ± 0.031
	26	-21.9 ± 1.9	0.530 ± 0.043	30	-22.9 ± 2.2	0.555 ± 0.050	$\mathbf{-21.2 \pm 1.7}$	$\mathbf{0.518 \pm 0.039}$
				Mean Balmer-lines time lag				
D	58	-20.4 ± 2.2	0.496 ± 0.049	47	-23.1 ± 2.7	0.560 ± 0.060	-20.8 ± 1.8	0.509 ± 0.041
	35	-23.0 ± 2.9	0.554 ± 0.066	55	-24.4 ± 3.6	0.588 ± 0.082	-21.6 ± 2.4	0.526 ± 0.055
E	54	-19.7 ± 1.6	0.483 ± 0.036	34	-20.1 ± 1.9	0.494 ± 0.044	-19.9 ± 1.4	0.489 ± 0.033
	31	-20.6 ± 2.2	0.502 ± 0.050	41	-20.2 ± 2.7	0.494 ± 0.060	-20.0 ± 1.9	0.490 ± 0.043
C	51	-20.4 ± 1.4	0.498 ± 0.033	27	-21.6 ± 1.5	0.526 ± 0.034	-20.5 ± 1.3	0.502 ± 0.030
	28	-22.5 ± 1.9	0.546 ± 0.041	31	-23.2 ± 2.1	0.561 ± 0.047	-21.5 ± 1.7	0.524 ± 0.038

[a]N is the number of pairs of r–L measurements included in each fit.

[b]Scatter is given as percent of the measurement value of r.

Note. — Two rows are given for each set of data: the first row gives the fit results where multiple data sets for each object are treated individually, and the second row gives the fit results where multiple measurements are averaged together as described in the text. The fit values in bold face are the fit to the r–L relationship that is quoted throughout this paper. **A.** All reliable measurements for the reverberation-mapped AGN are included in this fit. Only the objects PG 0844+349, PG 1211+143, and NGC 4593 do not have a reliable Hβ time lag measurement. **B.** In addition to any objects that were excluded above, the low luminosity objects NGC 3516, IC 4329A, and NGC 7469 have been excluded from this fit, for reasons described in the text. **C.** NGC 3227, NGC 4051, and PG 2130+099, as well as objects mentioned above, have been excluded from this fit for reasons described in the text. **D.** All reverberation-mapped AGN were included in this fit. **E.** NGC 4593, NGC 3516, IC 4329A, and NGC 7469 are excluded from this fit for reasons described in the text.

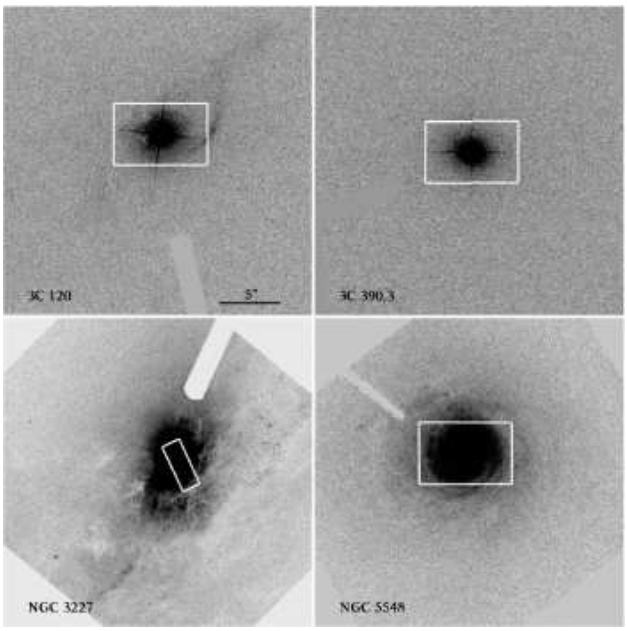

Fig. 1.— ACS HRC images of four representative galaxies from our sample: 3C 120, 3C 390.3, NGC 3227, and NGC 5548. Each galaxy is overlaid with the typical spectral aperture used in its original monitoring campaign, centered on the position of the AGN. North is up and east is to the left. The scale is the same for each of the images.

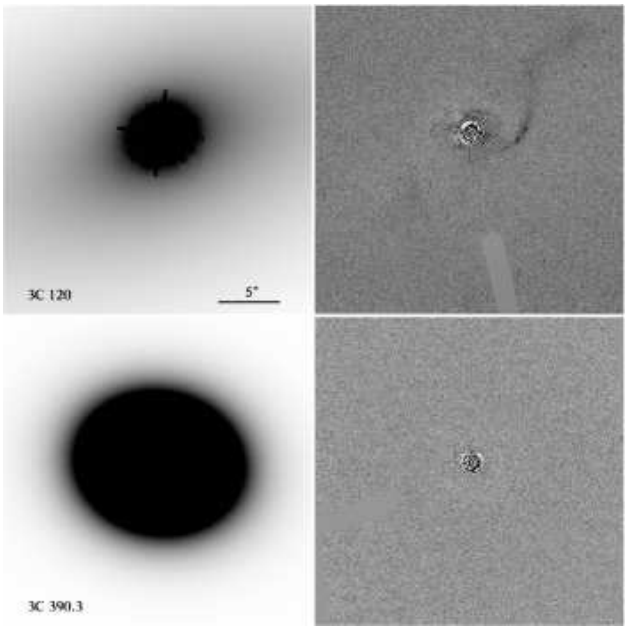

Fig. 2.— Galaxy+PSF models and residuals for four representative galaxies from our sample: 3C 120, 3C 390.3, NGC 3227, and NGC 5548. North is up and east is to the left. The scale is the same for each of the images.

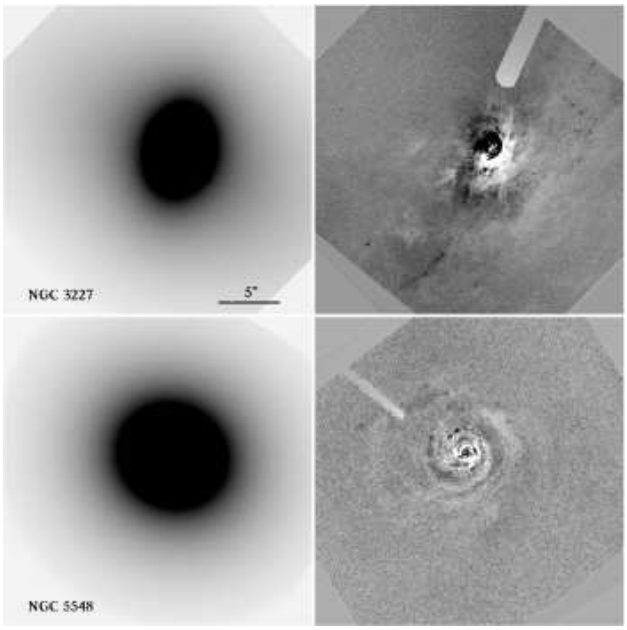

Fig. 2. — continued.

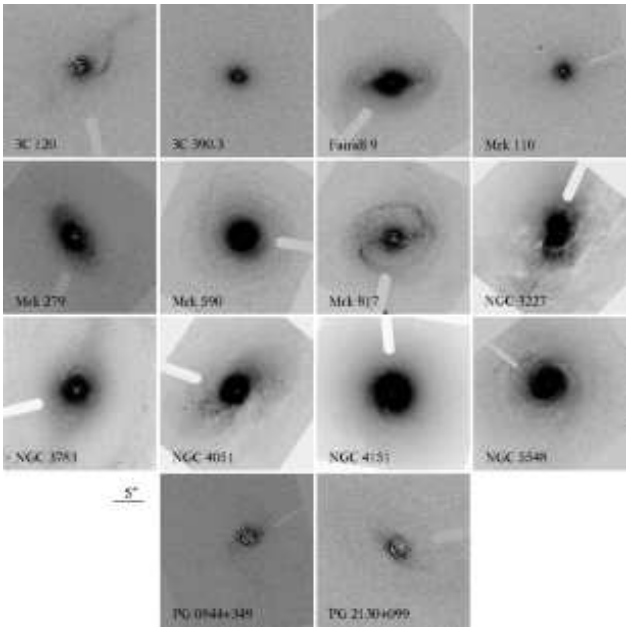

Fig. 3.— PSF-subtracted images for all 14 galaxies in this study. North is up and east is to the left. The scale is the same for each of the images.

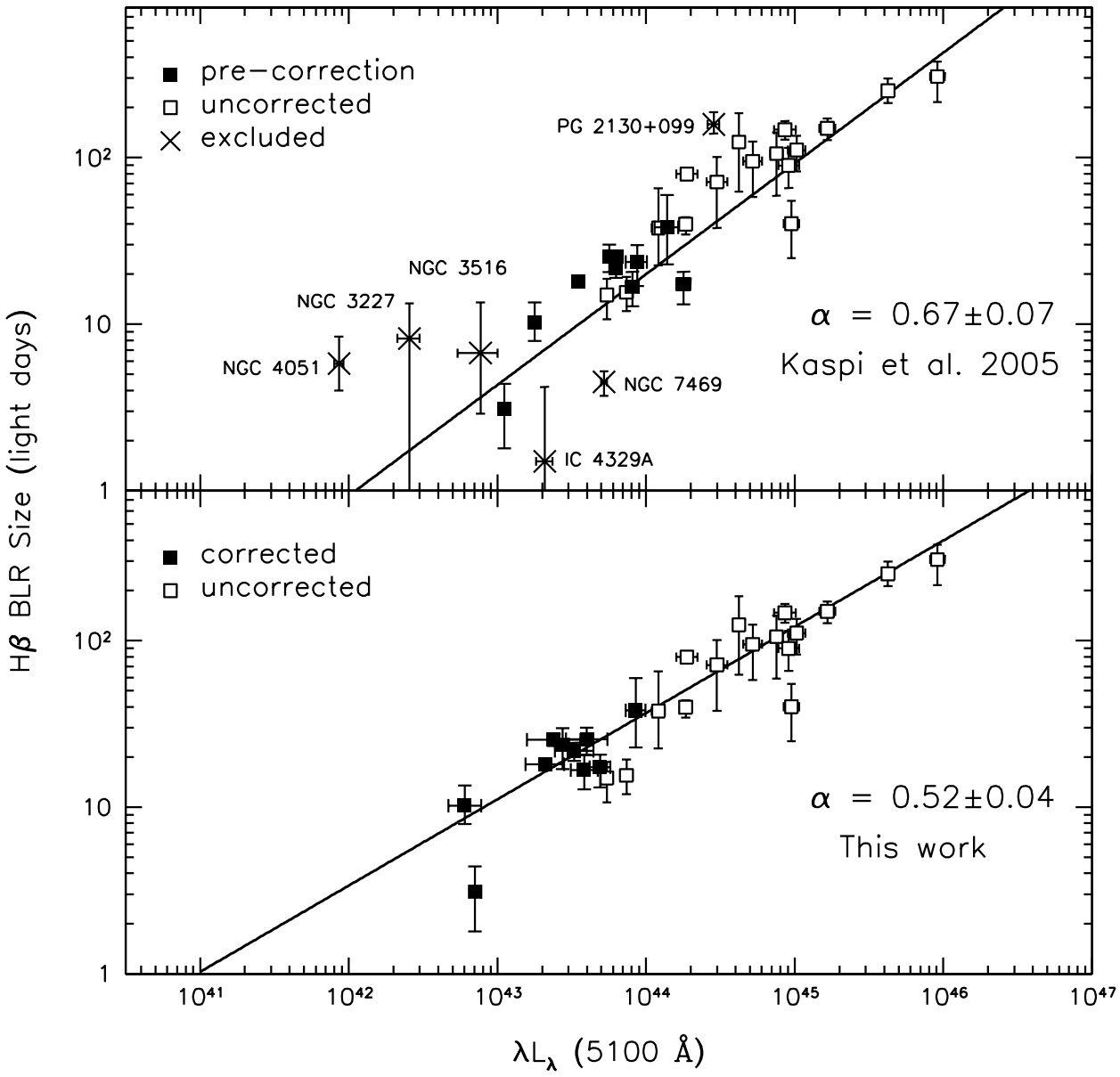

Fig. 4.— Hβ BLR size versus the luminosity at 5100 Å for the reverberation-mapped AGN. Open boxes are from Kaspi et al. (2005). Filled boxes are also from Kaspi et al. (2005), but are corrected for the host galaxy starlight contribution. The top fit is the power-law fit determined by Kaspi et al. (2005) and the bottom fit is the power-law fit determined in this work. The crosses show the locations of objects that were excluded from various fits for reasons described in the text.